Efficient Electromagnetic Scattering Simulation of Electrically Extra-Large Problems Using Phase Information and Adaptive Mesh Automation

Christian O. Díaz-Cáez, *Member, IEEE*, and Su Yan, *Senior Member, IEEE*

***Abstract*— In this article, an efficient simulation method is proposed to analyze extra-large electromagnetic scattering problems. With the incorporation of the traveling wave phase, the phase-extracted basis functions (PEBFs) can be defined on very large mesh elements, which effectively reduce the number of unknowns by two orders of magnitude, making it possible to simulate extra-large problems. Although the PEBFs were applied successfully in analyzing smooth and convex objects, they cannot accurately model the induced surface currents when geometrical singularities or strong mutual couplings are present. In such cases, the mesh elements must be small enough to describe the complicated amplitude variations accurately. One way to tackle this issue is to use a locally refined mesh. In this article, a set of rules is proposed, based on the geometrical and physical features of the problem, to identify elements that need to be locally refined. The mesh refinement is performed automatically based on the proposed rules, eliminating the need for human intervention. The discontinuous Galerkin integral equation (DGIE) method has been employed to handle the nonconformal mesh generated from the automatic mesh refinement. Numerical examples from smooth and nonsmooth objects are presented to demonstrate the performance of the method.**

***Index Terms*— Discontinuous Galerkin integral equation (DGIE), electromagnetic scattering problems, phase-extracted basis functions (PEBFs), standing wave, standing wave ratio (SWR), traveling wave.**

I. Introduction

IN ELECTROMAGNETIC scattering analysis using integral equations, basis functions are employed to interpolate the unknown induced currents. Most well-known basis functions, such as the divergence-conforming curvilinear Rao–Wilton–Glisson (CRWG) basis functions [1], are real-valued functions that only describe the induced surface current's amplitude. When solving a large-scale electromagnetic problem with such basis functions, many unknowns are required due to their limited ability to represent the phase variation of the unknown current, which can only be achieved through their complex expansion coefficients. To achieve a good descriptive accuracy of the phase variation across one wavelength of the current distribution, 10–20 basis functions are usually required. This significantly limits a method's simulation capability to solve electrically large problems. In this work, complex-valued phase-extracted basis functions (PEBFs) [2], [3], [4], [5], [6] are employed to describe unknown currents. By incorporating phase variation into the definition of basis functions, the PEBFs acquire excellent capability in describing phase changes of the unknown currents and can be defined on much larger elements. As a result, only two to three basis functions are needed to expand the current distribution across a wavelength, leading to a dramatic reduction of the total number of unknowns and a significant improvement of the simulation capability of the method of moments (MoMs).

The descriptive capacity of PEBFs has been demonstrated in scattering problems involving smooth and convex objects [2], [3]. When simulating nonsmooth objects with geometrical discontinuities, such as edges, corners, and tips, or concave objects that induce strong mutual couplings, the PEBFs lose their descriptive power because, in these cases, it is the strong amplitude variation that dominates the number of basis functions required per wavelength. Consequently, the PEBFs defined on large patches cannot model the amplitude variations properly. To accurately describe the induced currents in nonsmooth and/or concave cases, smaller mesh elements or higher-order basis functions can be used. The use of higher-order basis functions with PEBFs has been demonstrated in [4] and [5], while the application of locally refined mesh elements with PEBFs has not been reported. Local mesh refinement can be achieved by refining large mesh elements in areas that require small mesh elements, known as h-refinement.

In general, a denser mesh is used in a numerical simulation to provide better simulation accuracy but results in a higher computational cost. To achieve good overall simulation accuracy while maintaining low computational cost, a nonuniform mesh can be used. Here, a nonuniform mesh refers to the mesh configuration with larger elements in some simulation areas and smaller elements in some other areas. To generate such a mesh, physical insights, and user experiences are usually required. Several adaptive mesh refinement techniques have been developed [7], [8], [9], which are used mainly in the finite-element method (FEM) [10], to improve mesh quality and obtain a reliable numerical solution. Although

Manuscript received 15 August 2023; revised 14 March 2024; accepted 5 April 2024. Date of publication 2 May 2024; date of current version 7 June 2024. This work was supported by the National Science Foundation under Award 2101012 and Award 2238124. *(Corresponding author: Su Yan.)*

The authors are with the Department of Electrical Engineering and Computer Science, Howard University, Washington, DC 20059 USA (e-mail: christian.diaz@bison.howard.edu; su.yan@howard.edu).

Color versions of one or more figures in this article are available at https://doi.org/10.1109/TAP.2024.3393711.

Digital Object Identifier 10.1109/TAP.2024.3393711

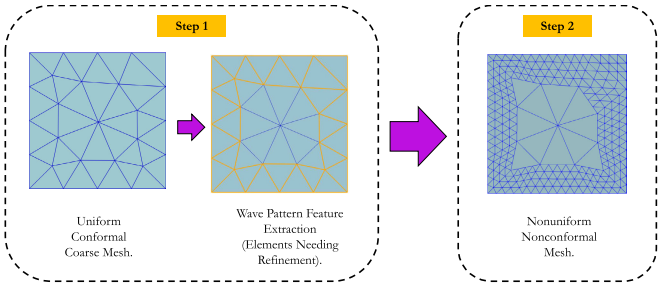

Fig. 1. Illustration of the MoM solution with the automated h-refinement. In Step 1, the feature of the induced current is extracted from a rough solution using a coarse conformal mesh. The elements that need refinement are identified. In Step 2, a local mesh refinement is performed to generate a nonconformal mesh, based on which an accurate solution can be obtained.

many refinement techniques have been developed for FEM, it was not until recently that new developments were made in the MoM solution of surface integral equations (SIEs) for electromagnetic scattering problems [11], [12], [13], [14], [15], [16], [17], [18]. These refinement methods are based on local error estimations using either the residual error of the SIEs or reference solution obtained from higher-order basis functions, based on which an iterative process is usually performed to generate a series of gradually refined meshes. Simulations employing these meshes are then performed to obtain numerical solutions with increasing accuracy. As a result, the overall computational cost of such an approach can be very high, especially when many iterations are needed to achieve convergence.

In this article, a novel two-step method is proposed to solve electrically extra-large problems very efficiently [19]. Instead of requiring repeated solutions to the problem with gradually refined meshes, only two solutions to the problem are needed, as illustrated in Fig. 1. First, a fast simulation of the problem using the PEBFs defined on a very coarse mesh is performed to obtain a rough solution of the induced currents. This can be completed very efficiently as a result of the very small number of unknowns involved. The rough solution of the induced currents is then processed by an identification method to locate the areas that need mesh refinement, which are referred to as the refining areas hereinafter. Such identification is based on the geometrical feature of the scatterer and the physical feature of the electromagnetic problem. The concept of standing wave ratio (SWR) has been utilized in this work to distinguish traveling from standing surface currents. Once identified, the elements are refined locally to construct a nonuniform and nonconformal mesh for the second solution of the problem, resulting in an accurate solution with a minimum computational cost. As will be shown in the numerical examples, the computational overhead of the proposed approach is very low, and the total computational time is much shorter than that of the traditional methods. To handle nonconformal mesh efficiently, a discontinuous Galerkin integral equation (DGIE) method [20], [21] is used with the PEBFs and the multilevel fast multipole algorithm (MLFMA) [22], [23] is used to accelerate the solution. While the use of the SWR concept in mesh refinement identification was proposed in [24], [25], and [26], its cohesive integration with PEBFs, DGIE, and MLFMA is detailed in this work, representing a significant step forward from our earlier work. The analysis and applications of the proposed method to solve large and complex problems have been presented in this article to showcase the method's versatility and wide applicability in electromagnetic scattering analysis.

II. Formulations

In this section, the PEBFs for solving electromagnetic scattering from smooth and convex objects are first reviewed, followed by the application of PEBFs in the context of the DGIE solution of integral equations. This covers the rough and improved solutions on the coarse and refined meshes, respectively, as illustrated in Fig. 1. Adaptive mesh refinement strategies will be introduced in Section III.

A. Phase-Extracted Basis Function

To reduce the number of unknowns in an electromagnetic calculation, much effort has been devoted to the development of new basis functions since three decades ago. Different basis functions have been proposed on the basis of analytical expressions or numerical solutions. One well-known example is the higher-order hierarchical basis functions based on the modified Legendre polynomials [27]. When the order is relatively high, the hierarchical basis functions can be defined on mesh elements as large as two wavelengths. However, the increasing order also leads to a rapid increase in the number of basis functions. Approximately 30 basis functions and the same number of unknown coefficients are needed within one square wavelength on the surface of a smooth perfectly electric conducting (PEC) object. Furthermore, as the order increases, the convergence of the iterative solution becomes slower. On the other hand, low-order basis functions, such as the CRWG basis functions, cannot be applied to large mesh elements due to the limited capability to describe the phase variation of the surface currents. One common issue of both types of basis functions is that they are both real-valued, leaving the phase variation of the current to be described only by their complex expansion coefficients. As a result, the number of basis functions on a unit area of the surface has to be maintained at a remarkably high level.

Based on such understandings, the number of basis functions is expected to be reduced dramatically if the basis functions are capable of properly describing the induced currents' phase distribution. As theoretically proven in [2], the induced surface currents in a PEC scattering problem have a phase dependence as same as that of the incident plane wave

$$\boldsymbol{J} \sim \mathrm{e}^{\mathrm{i}\boldsymbol{k}^{\mathrm{inc}}\cdot\boldsymbol{r}} \tag{1}$$

if the surface of the scatterer is smooth and convex. In (1), $\boldsymbol{k}^{\mathrm{inc}} = k_0\hat{\boldsymbol{k}}^{\mathrm{inc}}$ represents the vector wavenumber of the incident plane wave with k_0 and $\hat{\boldsymbol{k}}^{\mathrm{inc}}$ being the wavenumber and incident wave vector in free space, respectively, and $\boldsymbol{r}$ stands for a point on the surface of the scatterer. Separating the dominant plane-wave phase dependence from the induced surface currents $\boldsymbol{J}(\boldsymbol{r})$ leads to [2], [3], and [4]

$$\boldsymbol{J}(\boldsymbol{r}) = \boldsymbol{j}(\boldsymbol{r})\mathrm{e}^{\mathrm{i}\boldsymbol{k}^{\mathrm{inc}}\cdot\boldsymbol{r}} \tag{2}$$

with $\boldsymbol{j}(\boldsymbol{r})$ being the amplitude-dominant function, which can be approximated as the linear superposition of the CRWG basis function $\boldsymbol{j}_n(\boldsymbol{r})$ as

$$\boldsymbol{j} = \sum_{n=1}^{N} a_n \, \boldsymbol{j}_n(\boldsymbol{r}). \tag{3}$$

The induced current can finally be expanded as

$$\boldsymbol{J}(\boldsymbol{r}) = \sum_{n=1}^{N} a_n \, \boldsymbol{j}_n(\boldsymbol{r}) \mathrm{e}^{\mathrm{i}\boldsymbol{k}^{\mathrm{inc}}\cdot\boldsymbol{r}} \tag{4}$$

in which $\boldsymbol{j}_n(\boldsymbol{r})\mathrm{e}^{\mathrm{i}\boldsymbol{k}^{\mathrm{inc}}\cdot\boldsymbol{r}}$ is known as the PEBF.

The application of PEBFs in MoM is similar to that of conventional CRWG basis functions. When the Galerkin method is used, $\boldsymbol{v}_m(\boldsymbol{r})\mathrm{e}^{-\mathrm{i}\boldsymbol{k}^{\mathrm{inc}}\cdot\boldsymbol{r}}$ is used as a testing function. Implementation details can be found in [2] and [3].

B. DGIE Solution With PEBFs

The PEBFs described above work very well when the scatterers are smooth convex objects. When nonsmooth or concave surfaces are encountered, the wave reflection and mutual coupling destroy the nice behavior of the traveling wave phase variation of the induced surface currents. As a result, PEBFs can no longer be defined on very large mesh elements. To properly describe induced currents, larger mesh elements can be used in areas dominated by traveling waves, and smaller mesh elements can be used in areas dominated by standing waves. An automatic mesh refinement procedure will be detailed in Section III to construct such a nonuniform and nonconformal mesh since it is easier to generate and involves less number of elements compared to a similar nonuniform but conformal mesh. To process the nonconformal mesh, the DGIE method [20] is employed in this work. Unlike [20], where half RWG basis functions defined on single triangular elements are used throughout the mesh, half PEBFs are defined only along the nonconformal interfaces of the mesh in this work. In the conformal regions, full PEBFs defined on pairs of triangles are still used. Along the nonconformal interfaces, the discontinuous Galerkin method weakly enforces the normal current continuity by permitting and penalizing a slight normal current discontinuity along the interfaces.

Consider the combined-field integral equation (CFIE) [28]

$$\begin{aligned}\frac{\boldsymbol{J}}{2} - \mathrm{P.V.}\int_{S'} \hat{\boldsymbol{n}} \times \nabla G_0 \times \boldsymbol{J}\,\mathrm{d}\boldsymbol{r}' - \hat{\boldsymbol{n}}\times\hat{\boldsymbol{n}} \\ \times \int_{S'} \mathrm{i}k_0 \left(G_0 \boldsymbol{J} + \frac{1}{k_0^2}\nabla\nabla G_0 \cdot \boldsymbol{J}\right)\mathrm{d}\boldsymbol{r}' \\ = \hat{\boldsymbol{n}} \times \boldsymbol{H}^{\mathrm{inc}} + \hat{\boldsymbol{n}}\times\hat{\boldsymbol{n}} \times \frac{1}{\eta_0}\boldsymbol{E}^{\mathrm{inc}}\end{aligned} \tag{5}$$

where the magnetic-field integral equation (MFIE) and the electric-field integral equation (EFIE) are equally weighted. In (5), $G_0 = \mathrm{e}^{\mathrm{i}k_0|\boldsymbol{r}-\boldsymbol{r}'|}/4\pi|\boldsymbol{r}-\boldsymbol{r}'|$ stands for the scalar Green's function in free space with the wavenumber k_0, η_0 stands for the wave impedance in free space, and P.V. stands for the Cauchy principal value integration.

Using half RWG basis functions and the interior penalty presented in [20] along the nonconformal elemental interfaces, the CFIE can be discretized as

$$\begin{aligned}\sum_{n=1}^{N}\Bigg\{ &\frac{1}{2}\int_S \boldsymbol{v}_m\cdot\boldsymbol{j}_n\,\mathrm{d}\boldsymbol{r} - \mathrm{P.V.}\int_S\int_{S'} \boldsymbol{v}_m\cdot\hat{\boldsymbol{n}}\times\nabla G_0\times\boldsymbol{j}_n\,\mathrm{d}\boldsymbol{r}'\,\mathrm{d}\boldsymbol{r} \\ &+ \mathrm{i}k_0\int_S\int_{S'} G_0\left(\boldsymbol{v}_m\cdot\boldsymbol{j}_n - \frac{1}{k_0^2}\nabla\cdot\boldsymbol{v}_m\nabla'\cdot\boldsymbol{j}_n\right)\mathrm{d}\boldsymbol{r}'\,\mathrm{d}\boldsymbol{r} \\ &+ \frac{\mathrm{i}}{k_0}\oint_C\int_{S'} \hat{\boldsymbol{t}}_m\cdot\boldsymbol{v}_m\,\nabla'\cdot\boldsymbol{j}_n\,G_0\,\mathrm{d}\boldsymbol{r}'\,\mathrm{d}\ell \\ &+ \frac{\mathrm{i}}{k_0}\int_S\oint_{C'} \nabla\cdot\boldsymbol{v}_m\,\hat{\boldsymbol{t}}_n\cdot\boldsymbol{j}_n\,G_0\,\mathrm{d}\ell'\,\mathrm{d}\boldsymbol{r} \\ &- \beta\frac{\mathrm{i}}{k_0}\int_{C_{mn}} \hat{\boldsymbol{t}}_m\cdot\boldsymbol{v}_m\left(\hat{\boldsymbol{t}}_{mn}\cdot\boldsymbol{j}_m + \hat{\boldsymbol{t}}_{nm}\cdot\boldsymbol{j}_n\right)\mathrm{d}\ell\Bigg\} a_n \\ = &\int_S \boldsymbol{v}_m\cdot\left(\hat{\boldsymbol{n}}\times\boldsymbol{H}^{\mathrm{inc}} + \frac{1}{\eta_0}\boldsymbol{E}^{\mathrm{inc}}\right)\mathrm{d}\boldsymbol{r} \quad (\forall m\in[1,N])\end{aligned} \tag{6}$$

where $\boldsymbol{v}$, $\boldsymbol{j}$, $\hat{\boldsymbol{t}}$, and β denote the testing function, basis function, outward pointing unit normal vector on triangular boundaries as shown in Fig. 2, and the penalty/stabilization coefficient presented in [20], respectively.

When PE basis functions $\boldsymbol{j}\mathrm{e}^{\mathrm{i}\boldsymbol{k}^{\mathrm{inc}}\cdot\boldsymbol{r}'}$ and testing functions $\boldsymbol{v}\mathrm{e}^{-\mathrm{i}\boldsymbol{k}^{\mathrm{inc}}\cdot\boldsymbol{r}}$ are employed in the discretization of the CFIE using the DGIE method, the discretized system becomes

$$\sum_{n=1}^{N}\{A^1_{mn} + A^2_{mn} + A^3_{mn}\}a_n = V_m \quad (\forall m\in[1,N]) \tag{7}$$

where

$$\begin{aligned}A^1_{mn} = &\frac{1}{2}\int_S \boldsymbol{v}_m\cdot\boldsymbol{j}_n\,\mathrm{d}\boldsymbol{r} \\ &- \mathrm{P.V.}\int_S\int_{S'} g\,\boldsymbol{v}_m\cdot\hat{\boldsymbol{n}}\times\nabla G_0\times\boldsymbol{j}_n\,\mathrm{d}\boldsymbol{r}'\,\mathrm{d}\boldsymbol{r}\end{aligned} \tag{8}$$

$$\begin{aligned}A^2_{mn} = &\mathrm{i}k_0\int_S\int_{S'} g\,G_0\Bigg[\boldsymbol{v}_m\cdot\boldsymbol{j}_n - \hat{\boldsymbol{k}}^{\mathrm{inc}}\cdot\boldsymbol{v}_m\,\hat{\boldsymbol{k}}^{\mathrm{inc}}\cdot\boldsymbol{j}_n \\ &- \frac{\mathrm{i}}{k_0}\left(\nabla\cdot\boldsymbol{v}_m\,\hat{\boldsymbol{k}}^{\mathrm{inc}}\cdot\boldsymbol{j}_n - \hat{\boldsymbol{k}}^{\mathrm{inc}}\cdot\boldsymbol{v}_m\,\nabla'\cdot\boldsymbol{j}_n\right) \\ &- \frac{1}{k_0^2}\nabla\cdot\boldsymbol{v}_m\nabla'\cdot\boldsymbol{j}_n\Bigg]\mathrm{d}\boldsymbol{r}'\,\mathrm{d}\boldsymbol{r} \\ &+ \oint_C\int_{S'} g\,G_0\,\hat{\boldsymbol{t}}_m\cdot\boldsymbol{v}_m\left(\frac{\mathrm{i}}{k_0}\nabla'\cdot\boldsymbol{j}_n - \hat{\boldsymbol{k}}^{\mathrm{inc}}\cdot\boldsymbol{j}_n\right)\mathrm{d}\boldsymbol{r}'\,\mathrm{d}\ell \\ &+ \int_S\oint_{C'} g\,G_0\left(\frac{\mathrm{i}}{k_0}\nabla\cdot\boldsymbol{v}_m + \hat{\boldsymbol{k}}^{\mathrm{inc}}\cdot\boldsymbol{v}_m\right)\hat{\boldsymbol{t}}_n\cdot\boldsymbol{j}_n\,\mathrm{d}\ell'\,\mathrm{d}\boldsymbol{r}\end{aligned} \tag{9}$$

$$A^3_{mn} = -\beta\frac{\mathrm{i}}{k_0}\int_{C_{mn}} \hat{\boldsymbol{t}}_m\cdot\boldsymbol{v}_m\left(\hat{\boldsymbol{t}}_{mn}\cdot\boldsymbol{j}_m + \hat{\boldsymbol{t}}_{nm}\cdot\boldsymbol{j}_n\right)\mathrm{d}\ell \tag{10}$$

$$V_m = \frac{1}{\eta_0}\int_S \boldsymbol{v}_m\cdot\left(\hat{\boldsymbol{n}}\times\hat{\boldsymbol{h}}^i + \hat{\boldsymbol{e}}^i\right)\mathrm{d}\boldsymbol{r}. \tag{11}$$

In (8) and (9), $g = \mathrm{e}^{\mathrm{i}\boldsymbol{k}^{\mathrm{inc}}\cdot(\boldsymbol{r}'-\boldsymbol{r})}$, while in (11), $\hat{\boldsymbol{h}}^i$ and $\hat{\boldsymbol{e}}^i$ denote the polarization vector of the incident magnetic and electric fields, respectively. In these expressions, A^1_{mn} is obtained by discretizing the MFIE operator, A^2_{mn} is obtained from the EFIE operator, which involves a contour integration when either the basis or the testing function is a half PE function, and A^3_{mn} is the contour penalty term that penalizes

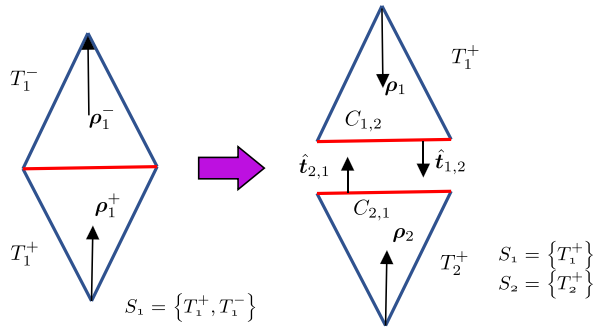

Fig. 2. Schematic of the half RWG basis functions defined on conformal elements. A full RWG function is divided into two half RWG basis functions along the common edge highlighted in red.

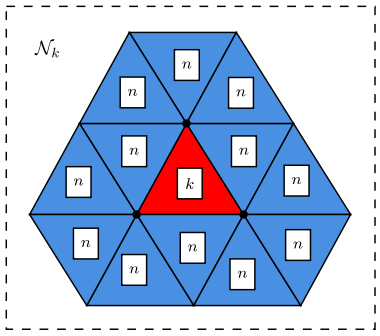

Fig. 3. Neighborhood $\mathcal{N}_k$ of triangle k. Direct neighbors are those sharing a node with triangle k, labeled as n.

any normal discontinuity of the induced current. Equation (7) can then be solved iteratively using either the MoM or the MLFMA [22], [23].

III. Adaptive Mesh Refinement Based on Geometrical and Physical Features

As illustrated in Fig. 1, a two-step approach is proposed to identify the refining areas automatically. In the first step, a coarse mesh is used in the MoM solution to obtain a rough solution quickly using the PEBFs. In this work, two to three mesh elements per wavelength are used in constructing such a coarse mesh. If the induced surface currents are traveling wave-dominant, the PEBFs can describe their phase variations properly. This will result in a slowly varying amplitude in the solution of the surface currents. In contrast, in cases where the induced surface currents are standing wave dominant, their amplitude varies drastically and cannot be expressed properly by PEBFs defined on large mesh elements. In such cases, the mesh elements must be refined such that the amplitude oscillations can be captured properly by PEBFs. Based on such a physical understanding, the SWR of the surface current can be employed to identify standing wave-dominant areas. The SWR in the triangular element k is defined and estimated as

$$\mathrm{SWR}(k) = \frac{\max_{\forall i \in \mathcal{N}_k} \|\boldsymbol{J}(\boldsymbol{r}_i)\|}{\min_{\forall i \in \mathcal{N}_k} \|\boldsymbol{J}(\boldsymbol{r}_i)\|} \tag{12}$$

where $\mathcal{N}_k$ denotes triangle k and its direct neighbors as illustrated in Fig. 3 and $\boldsymbol{J}$ can be calculated using the rough solutions obtained by the PEBFs defined on the coarse mesh. The selection of the mesh density should balance two factors. First, the element size should be relatively small so that the rough solution can capture important variations of the surface currents, leading to reasonable SWR estimations. Second, the element size should be relatively large to reduce the overall computational cost and ensure that the estimation of SWR is performed in a relatively large area. Taking into account these two factors, the initial mesh density is chosen as $\lambda/2.5$ in the rough first-step solution. As a result, the SWR is calculated for every triangular element in a neighborhood of approximately one wavelength in diameter. This ensures that a sufficiently large area is considered when estimating the SWR. A larger SWR indicates a stronger standing wave component, which requires a finer mesh to resolve the current amplitude variation [24], [25], [26]. If a neighborhood contains a purely traveling wave without any current reflection or mutual coupling, the SWR reaches its minimum value of one. It must be pointed out that the use of PEBFs in the rough solution is necessary because they describe the traveling wave phase explicitly, leaving a constant amplitude in a purely traveling wave case and resulting in the SWR being one. In the meanwhile, it has been demonstrated in [2], [3], [4], and [5] that the PEBFs can be defined on large mesh elements with a small number of unknowns without losing their expressive capability significantly. This is extremely important in obtaining a rough but reasonable solution with a low computational cost to have a fast and accurate estimation of the SWR. The use of traditional real-valued basis functions, such as the CRWG basis functions, cannot achieve these goals.

The SWR is an indicator of the physical characteristics of the problem, which accounts for the frequency, polarization, and direction of incidence of the incident wave. It is also an indicator of the geometrical features of the problem, which accounts for multiple reflections and mutual couplings of the wave due to the geometrical structure of the scatterer. In addition, other geometrical features must also be considered. This mainly includes the geometrical discontinuities, such as geometrical edges, corners, and tips, that can cause strong current reflection or edge singularity. In such cases, a finer local mesh is also required to provide a good geometrical and physical resolution. In summary, the following set of three rules is proposed to identify the refining areas in the initial coarse mesh. Specifically, when an element: 1) is associated with an open geometrical boundary; 2) is located at a geometrical discontinuity (e.g., edges, corners, or tips); and 3) has an SWR higher than a preset threshold κ, and has a current amplitude greater than a preset percentage ξ of the maximum current amplitude in the entire simulation domain, the element needs to be refined. In this work, $\kappa = 10$ and $\xi = 1\%$ are used. The values of these parameters are selected after extensive numerical examples by considering the balance and tradeoff between numerical accuracy and computational efficiency. The use of parameter ξ ensures that elements with very small current amplitudes, for example, those in the shadow region, do not get refined even if they satisfy one of the above three rules, since their overall contribution to the radar cross section (RCS) is insignificant.

Together, Rules 1 and 2 apply to both open and closed objects to identify elements at geometrical discontinuities that induce current reflections and singularities. To identify

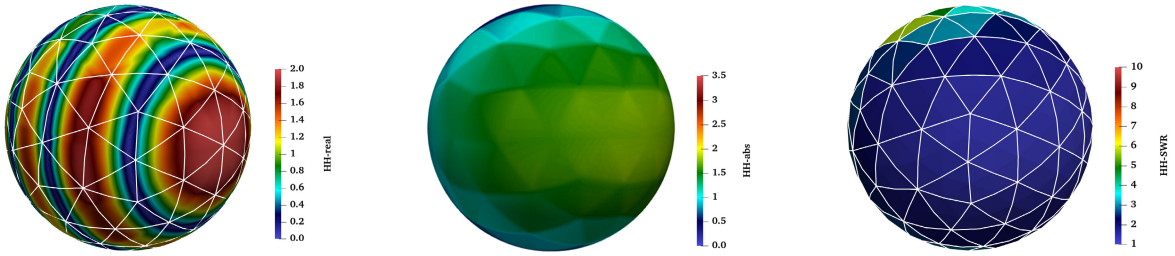

(a) (b) (c)

Fig. 4. Numerical results from the PEC sphere scattering example. (a) Real part. (b) Amplitude. (c) SWR of the induced current on the PEC sphere with a radius of 1 m.

geometrical discontinuities, the angle θ between the normal directions of two adjacent elements can be calculated. When $\theta \geq (\pi/4)$, the two adjacent elements constitute a geometrical discontinuity and need to be refined.

It is important to note that the concept of SWR is specifically employed with the application of the PEBFs, which describes only traveling waves properly on smooth and convex objects. What cannot be properly described include singular currents along geometrical discontinuities and strongly standing-wave-dominant currents. In the above rules, Rules 1 and 2 identify geometrical discontinuities while Rule 3 captures excitation- and geometry-related multiple reflections and mutual couplings.

Once all refining areas are identified, the mesh elements in those areas can be refined automatically in the computational code without the need for any third-party mesh generator or human intervention. In this work, the mesh refinement is done by connecting the midpoints of three edges of a triangle, so one triangle is refined to four. This procedure is done twice for all identified triangles so that one original triangle is refined into 16 smaller ones. The scattering problem will then be solved again using PEBFs defined on the nonuniform and nonconformal mesh and the DGIE method presented in Section II-B. In our numerical examples that will be presented in Section IV, the initial coarse mesh has a mesh density of $\lambda/2.5$. After mesh refinement, each small triangle is approximately $\lambda/10$ in size. Employing PEBFs on such small triangles is almost the same as using traditional CRWG basis functions up to a difference of a constant phase factor. Therefore, there is no need to use CRWG basis functions on the refined elements, for the sake of implementation simplicity.

IV. Numerical Examples

In this section, several numerical examples are given to demonstrate the accuracy, efficiency, and capability of the proposed algorithm in the numerical simulation of electromagnetic scattering problems. Since either MoM or MLFMA is used in solving the scattering problems, the computational complexities are $\mathcal{O}(N^2)$ or $\mathcal{O}(N\log N)$, respectively, with N being the total number of unknowns.

A. Validation Examples

In this section, three examples are particularly designed and presented to demonstrate the effectiveness of the proposed method in distinguishing standing waves from traveling waves. The first example is a PEC sphere, which is the simplest and smoothest object. It is used here to demonstrate the traveling-wave-dominant case. The second example is a PEC plate, which is an open target and has edges that can cause current reflection. This example is designed to demonstrate a standing wave caused by geometrical discontinuities. The last example is a PEC corner reflector, which is a concave object with many edges that can cause multiple current reflections and strong mutual couplings. It is a standing wave-dominant case.

1) PEC Sphere: As the first example, a PEC sphere with a radius of 1 m is illuminated by a 300-MHz plane wave. Obtained from the CFIE and PEBFs defined on triangular elements of size $\lambda/2.5$, the real part and amplitude of the surface current distribution are shown in Fig. 4(a) and (b), respectively. From Fig. 4(b), a very smooth and uniform current amplitude is observed, indicating a traveling-wave characteristic. This is verified by the SWR values shown in Fig. 4(c), which are all smaller than the preset threshold of $\kappa = 10$. According to the proposed rules, no refinement is needed for this example. Due to the use of the PEBFs, a total of only 258 unknowns are involved in the simulation. As defined in (13), the relative root-mean-square (rms) error of the calculated RCS (not shown in the article) is only 4.88% compared to the Mie series solution

$$\text{rRMS} = \sqrt{\frac{\sum_{p=1}^{N}\left|\sigma^{\text{cal}}(\hat{r}_p) - \sigma^{\text{ref}}(\hat{r}_p)\right|^2}{\sum_{p=1}^{N}\left[\sigma^{\text{ref}}(\hat{r}_p)\right]^2}}. \tag{13}$$

In (13), N is the number of scattering angles and $\sigma^{\text{cal}}(\hat{\boldsymbol{r}})$ and $\sigma^{\text{ref}}(\hat{\boldsymbol{r}})$ are the calculated and reference RCS at the pth scattering angle in the direction of $\hat{\boldsymbol{r}}_p$, respectively.

2) PEC Plate: In the next example, a 5-by-5 m^2 PEC plate is illuminated by a 300-MHz incident plane wave. Since it is an open object, the EFIE is employed to solve the scattering problem. The induced current obtained by solving the problem with CRWG basis functions defined on a dense mesh with a mesh size of $\lambda/10$ and 8555 unknowns is used as the reference solution and presented in Fig. 5(a). Using the proposed method, this problem is first solved with PEBFs defined on a coarse mesh with a mesh size of $\lambda/2.5$ and 559 unknowns, as shown in Fig. 5(e). The rough solution is shown in Fig. 5(b) based on which the SWR is calculated and shown in Fig. 5(d), where elements with SWR values greater than 10 are shown in red. Apparently, the large SWR values in this case correspond to a strong current reflection from both vertical edges of the

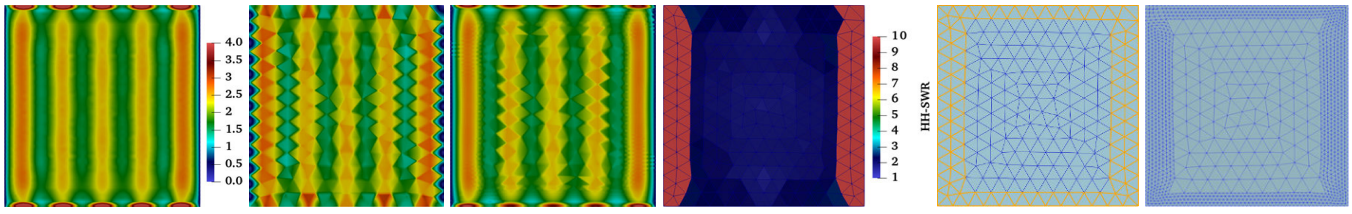

Fig. 5. Numerical results from the 5-by-5 m^2 PEC plate scattering example. The amplitude of the induced surface currents obtained from (a) CRWG basis functions defined on a dense mesh with an average mesh size of $\lambda/10$, (b) PEBFs defined on a coarse mesh with an average mesh size of $\lambda/2.5$ shown in (e), and (c) PEBFs defined on the mesh shown in (f). (d) SWR of the induced current on the PEC plate based on the solution in (b). (e) Identified triangular elements are to be refined as highlighted in orange. (f) Refined nonuniform and nonconformal mesh.

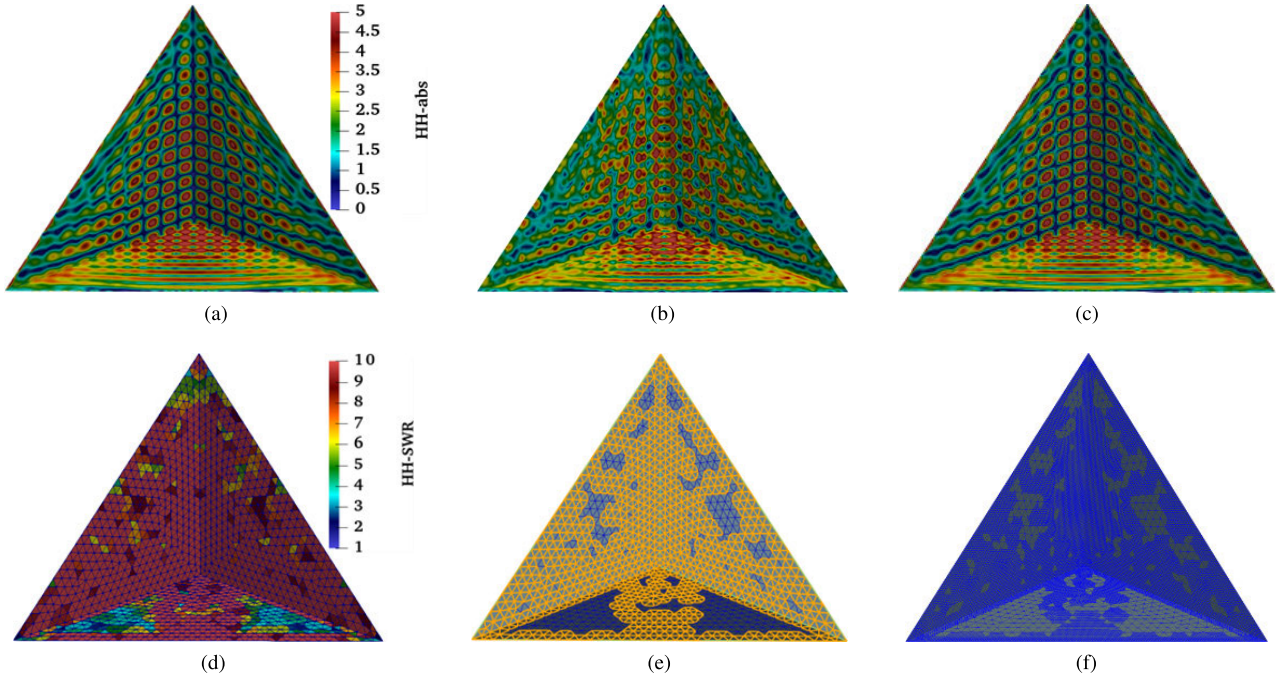

Fig. 6. Numerical results from the PEC corner reflector scattering example. The amplitude of the induced surface currents obtained from (a) CRWG basis functions defined on a dense mesh with an average mesh size of $\lambda/10$, (b) PEBFs defined on a coarse mesh with an average mesh size of $\lambda/2.5$ shown in (e), and (c) PEBFs defined on the mesh shown in (f). (d) SWR of the induced current on the PEC corner reflector based on the solution in (b). (e) Identified triangular elements are to be refined as highlighted in orange. (f) Refined nonuniform and nonconformal mesh.

plate. According to the set of rules proposed in this article, elements that require refinements are highlighted in orange in Fig. 5(e), and the automatically refined mesh is shown in Fig. 5(f), resulting in a total of 3826 unknowns. Based on such a nonuniform and nonconformal mesh, the scattering problem is solved again with PEBFs. The improved current solution is shown in Fig. 5(c). The RCS values calculated in these two steps have a relative rms error of 6.81% and 1.83%, respectively, using the CRWG solution on the dense mesh as a reference.

3) A PEC Corner Reflector: The third validation example concerns a trihedral PEC corner reflector with an edge length of 10 m and excited by a 300-MHz plane wave that illuminates its concave side. This corner reflector consists of three mutually perpendicular, intersecting flat surfaces that directly reflect the incident electromagnetic wave back toward the emission source. It is a useful device for the calibration of the radar system and is usually used as a retroreflector. Fig. 6(a)–(c) presents the current amplitude distributions obtained with the CRWG basis functions defined on a dense mesh, the PEBFs defined on a coarse mesh, and the PEBFs defined on a refined mesh, respectively. Clearly, the PEBFs defined on

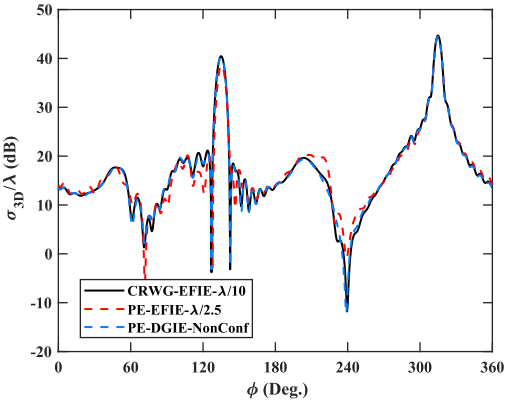

Fig. 7. Bistatic RCS of the PEC corner reflector at 300 MHz.

large triangles cannot capture the strong amplitude oscillation since the low-order function, the CRWG function, is used to account for the amplitude variation in the PEBFs. The refined solution shown in Fig. 6(c) resembles that in Fig. 6(a) much better, indicating a much-improved solution accuracy. This is also confirmed in Fig. 7 which shows the comparison of the RCS results obtained from these three cases. Using the

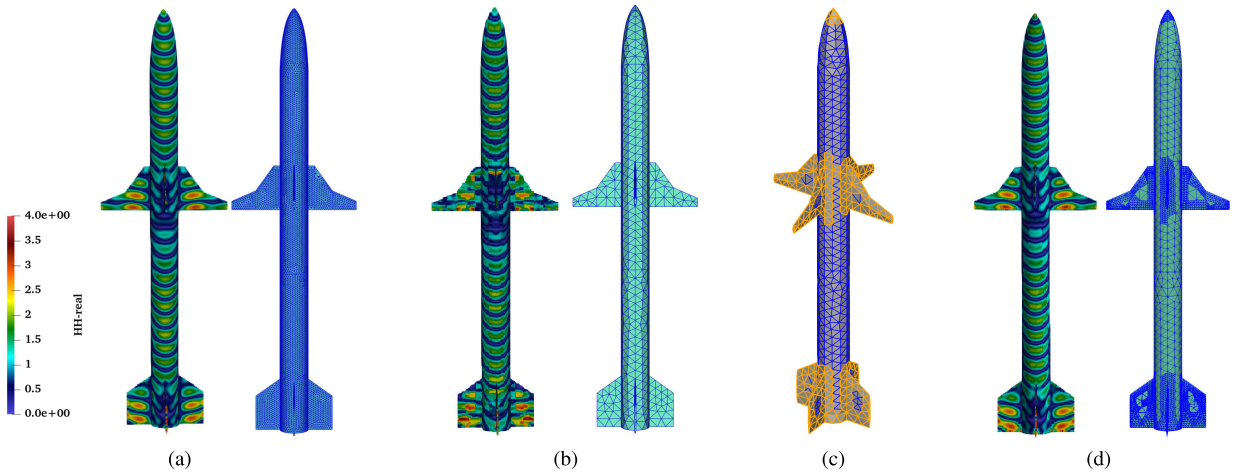

Fig. 8. Geometrical discretizations and induced current distributions over the surface of a missile-like object using (a) CRWG basis functions defined on a dense mesh with an average mesh size of $\lambda/10$, (b) PEBFs defined on a coarse mesh with an average mesh size of $\lambda/2.5$, and (d) PEBFs defined on a nonuniform and nonconformal mesh. (c) Identified triangular elements are to be refined as highlighted in orange.

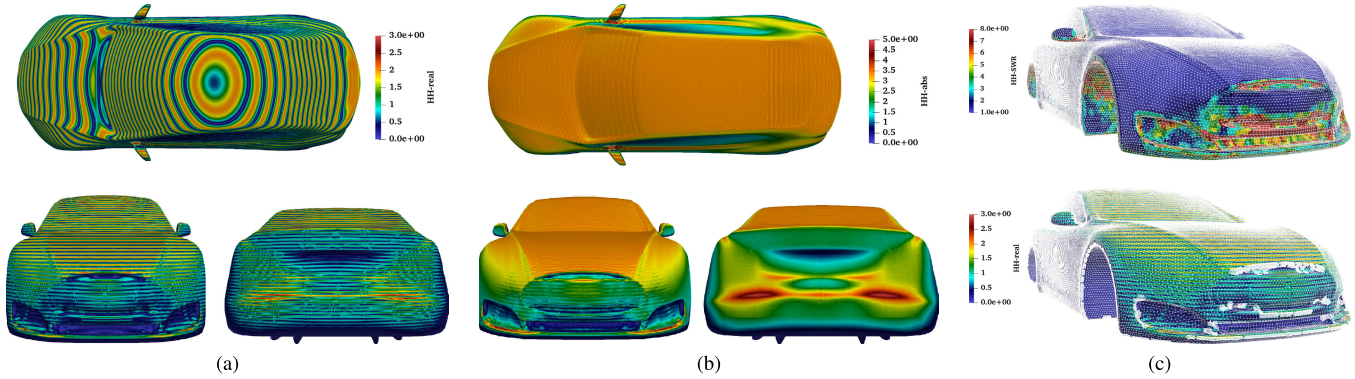

Fig. 9. Simulation results of the scattering from a PEC car at 6 GHz. (a) Real part and (b) amplitude of the surface current distribution. (c) SWR distribution (top) and nonconformal mesh after automatic mesh refinement (bottom).

CRWG results as a reference, the relative rms errors of the two PEBF results are 13.41% and 3.79%, respectively. Based on the solution shown in Fig. 6(b), the SWR is calculated and presented in Fig. 6(d). From this figure, it is obvious that most of the elements have SWR values larger than 10, indicating strong mutual couplings of the wave due to multiple reflections that create standing waves almost on the entire structure. Shown in Fig. 6(e) and (f) are the identified refining areas and the refined nonuniform and nonconformal mesh, respectively.

B. Scattering From a PEC Missile-Like Object

Electromagnetic scattering from a PEC missile-like object is presented in this section. With a total length of 4.7 m, this object is under the illumination of a 1.5-GHz VV-polarized incident plane wave coming toward its nose. The geometrical discretizations and the surface current distributions obtained using the CRWG basis functions defined on a dense mesh, the PEBFs defined on a uniform coarse mesh, and the PEBFs defined on a nonuniform and nonconformal mesh are presented in Fig. 8(a), (b), and (d), respectively. It is clear that the solution from the coarse mesh cannot resolve the strong induced current oscillation on the wings and tail fins. Shown in Fig. 8(c) are the highlighted refining areas identified by the proposed method. When the mesh is refined over the nose and all four wings and tail fins, the current distribution on the nonconformal mesh matches the reference CRWG solution very well. Evidently, the proposed method successfully identifies geometrical discontinuities and strong mutual coupling regions. From the bistatic RCS shown in Fig. 11(a), it can be seen that the nonuniform mesh results in a much more accurate solution than the coarse mesh. The computational data and the relative rms error of this example are presented in Table I. With the use of a coarse mesh, the rms error is as high as 51.5%. But when the adaptively refined mesh is used, the error is effectively reduced to 12.7%. This is a good demonstration of the application of a coarse mesh in the first step. Even though it results in a large rms error, it can still generate a reasonable estimation of SWR to capture all elements that need refinement. Furthermore, while the error 12.7% seems high, it can mostly be attributed to the differences of very small values around the dips of the highly oscillatory RCS curve, as observed in Fig. 11(a). From Table I, it is clear that the memory and the total CPU time requirements of the two PE solutions are significantly less than those of the CRWG solution. In this table and Tables II and III, the CPU time of the second step includes the time spent on calculating SWR and identifying geometrical singularities, since all these operations

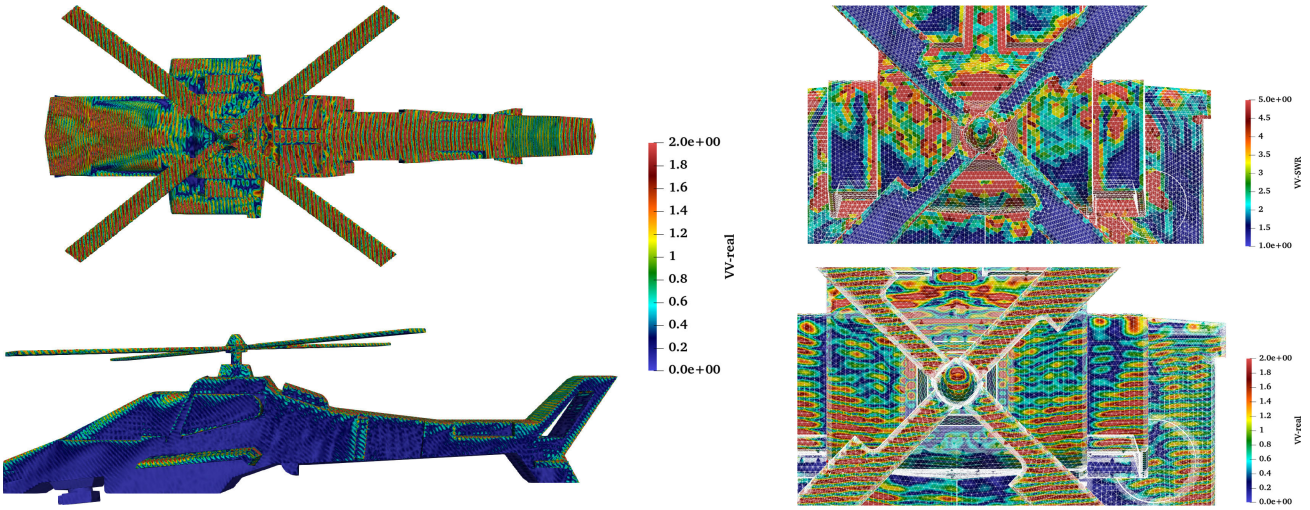

(a) (b)

Fig. 10. Simulation results of the scattering from a PEC helicopter at 6 GHz. (a) Top and side views of the induced surface current. (b) SWR distribution over a uniform and conformal coarse mesh (top) and zoomed-in view of the induced surface current over the locally refined mesh (bottom).

TABLE I

COMPARISON OF COMPUTATIONAL DATA AND RELATIVE RMS ERROR OF THE MISSILE SCATTERING AT 1.5 GHZ

Basis Function (Mesh Size)	No. of Unknowns	Memory (Mb)	Total CPU Time (sec.)	rRMS (%)
CRWG ($\lambda/10$)	44,736	2072.11	68	—
PE ($\lambda/2.5$)	2,817	61.07	3	51.5
PE (Nonuni.)	26,607	1309.87	19	12.7

TABLE II

COMPARISON OF COMPUTATIONAL DATA AND RELATIVE RMS ERROR OF THE CAR SCATTERING AT 6 GHZ

Basis Function (Mesh Size)	No. of Unknowns	Memory (Mb)	Total CPU Time (min.)	rRMS (%)
CRWG ($\lambda/10$)	3,951,816	35,890.50	247.9	—
PE ($\lambda/2.5$)	248,436	7,008.84	71.6	20.3
PE (Nonuni.)	384,391	8,571.52	101.9	16.2

are regarded as the preprocessing of the second step. The complexity of these operations is $\mathcal{O}(N)$.

C. Scattering From a PEC Car

An electrically larger problem is considered in this example as a 5-m-long PEC car, which is very similar to a Tesla model. A 6-GHz HH-polarized incident plane wave is coming from the top of the car at $\theta = 0°$ and $\phi = 0°$. At 6 GHz, the electrical size of the object is 100λ. The real part of the surface current distribution solved with PEBFs defined on the automatically refined nonconformal mesh is presented in Fig. 9(a) from different perspectives. Similarly, the amplitude of the current is presented in Fig. 9(b). The SWR distribution and the nonconformal mesh are presented in Fig. 9(c). In Fig. 11(b) and Table II, the bistatic RCS and the computational data are compared among the reference solution from CRWG basis functions on the dense mesh, PEBFs on the coarse mesh, and PEBFs on the refined mesh, respectively. From Table II, it is clear that the computational and storage requirements of the proposed method are smaller than those of the traditional method with CRWG basis functions. With the adaptive refined mesh, the number of unknowns and the relative rms error have been effectively reduced.

TABLE III

COMPARISON OF COMPUTATIONAL DATA OF THE HELICOPTER SCATTERING AT 6 GHZ

Basis Function (Mesh Size)	No. of Unknowns	Memory (Mb)	Total CPU Time (min.)
CRWG ($\lambda/10$)	3,857,210	28,966.10	N/C
PE ($\lambda/2.5$)	185,097	5,776.51	42.0
PE (Nonuni.)	796,147	11,786.80	94.0

D. Scattering From a PEC Helicopter

As the last example, electromagnetic scattering from a PEC helicopter is presented. This object has a physical length of 4.86 m and an electrical size of 97.2λ under the illumination of a 6-GHz VV-polarized incident plane wave coming from $\theta = 90°$ and $\phi = 45°$. Solved with the PEBFs, the surface current distribution on the object is presented in Fig. 10(a) from different viewing angles. The SWR distribution and the nonconformal mesh after the automatic mesh refinement are presented in Fig. 10(b), from which a complicated current distribution is observed, indicating multiple current reflections and mutual couplings. The numerical solution of this problem using the traditional method with CRWG basis functions failed to converge due to the large number of unknowns needed and the complex structure under consideration, which manifests the unique descriptive power of the PEBFs and the simulation capability of the proposed method. In Table III, the number of unknowns and the computational resources are summarized. In this table, "N/C" stands for not converged. The bistatic RCS is presented in Fig. 11(c), from which notable differences can be observed at scattering angles $\phi = 250°$, $290°$, and $340°$.

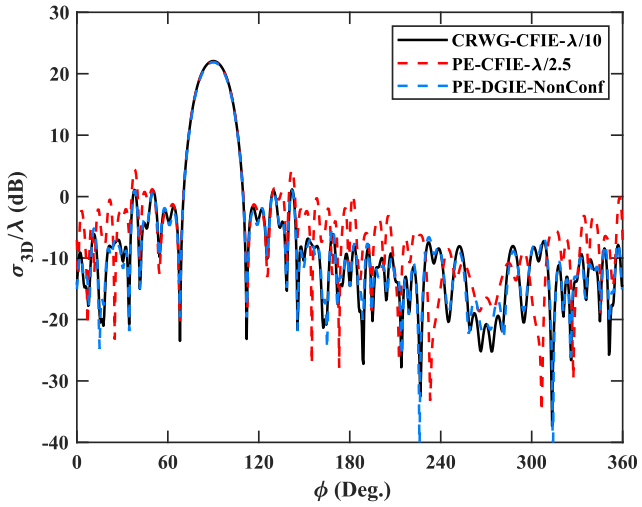

(a)

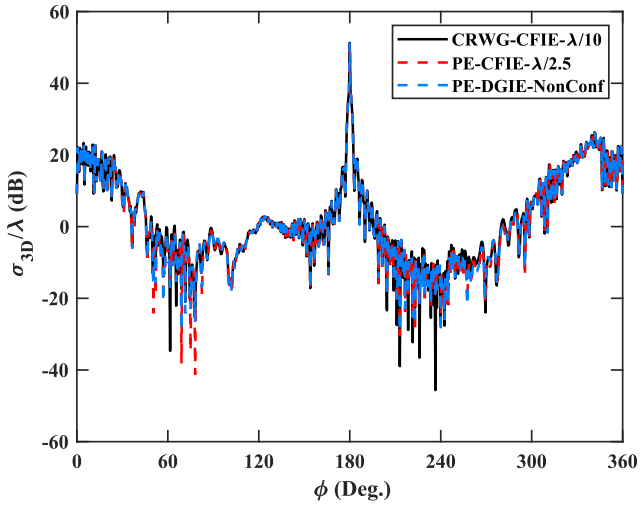

(b)

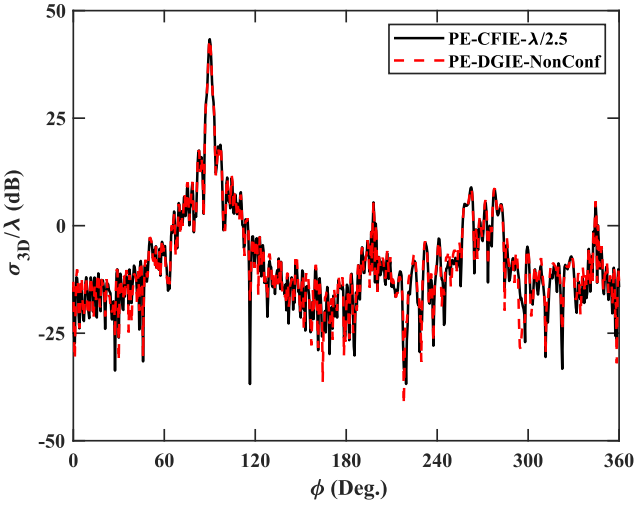

(c)

Fig. 11. Bistatic RCS of (a) missile-like object at 1.5 GHz, (b) PEC car at 6 GHz, and (c) PEC helicopter at 6 GHz.

V. Conclusion

In this article, a two-step adaptive mesh refinement method is proposed to solve electromagnetic scattering problems accurately and efficiently. Thanks to the proper description of the phase variation in the PEBFs, low-order amplitude functions can be employed and defined on very large mesh elements. The use of the PEBFs alone can readily solve scattering from smooth and convex objects accurately with much smaller computational and storage costs. When complicated objects involving nonsmooth and concave surfaces are considered, this work has proposed and demonstrated an efficient way to identify, from a rough solution on an initial coarse mesh, elements that require local refinements. This is made possible by the recognition of geometrical discontinuities and the investigation of the SWR of the induced surface currents. By automatically refining the identified elements, the scattering problems are solved again with PEBFs defined on the nonuniform and nonconformal mesh using the DGIE method. Multiple numerical examples have shown that even with two solutions, the proposed method still outperforms the traditional method with CRWG basis functions in terms of both memory and CPU time requirements and generates numerical solutions with an accuracy comparable to those of the traditional method. With the proposed method, the initial geometrical discretization can be obtained much more easily due to the use of a coarse mesh, which is then automatically refined in the simulation code without any human intervention. This work paves the way for a more intelligent algorithm that recognizes the geometrical and physical characteristics of a given problem and provides a powerful simulation tool that calculates electromagnetic scattering from extra-large objects accurately and efficiently.

References

[1] R. D. Graglia, D. R. Wilton, and A. F. Peterson, "Higher order interpolatory vector bases for computational electromagnetics," *IEEE Trans. Antennas Propag.*, vol. 45, no. 3, pp. 329–342, Mar. 1997.

[2] Z.-P. Nie, S. Yan, S. He, and J. Hu, "On the basis functions with traveling wave phase factor for efficient analysis of scattering from electrically large targets," *Prog. Electromagn. Res.*, vol. 85, pp. 83–114, 2008.

[3] S. Yan, S. He, Z.-P. Nie, and J. Hu, "Simulating wide band radar response from pec targets using phase extracted basis functions," *Prog. Electromagn. Res. B*, vol. 13, pp. 409–431, 2009.

[4] S. Yan, S. Ren, Z. Nie, S. He, and J. Hu, "Efficient analysis of electromagnetic scattering from electrically large complex objects by using phase-extracted basis functions," *IEEE Antennas Propag. Mag.*, vol. 54, no. 5, pp. 88–108, Oct. 2012.

[5] Z. Nie, S. Ren, S. Yan, S. He, and J. Hu, "Modified phase-extracted basis functions for efficient analysis of scattering from electrically large targets," *Proc. IEEE*, vol. 101, no. 2, pp. 401–413, Feb. 2013.

[6] K. Han, C. Fang, Y. Chen, and X. Que, "An efficient domain decomposition method using phase extracted basis functions," in *Proc. 12th Int. Symp. Antennas, Propag. EM Theory (ISAPE)*, Dec. 2018, pp. 1–2.

[7] P. Di Stolfo, A. Schröder, N. Zander, and S. Kollmannsberger, "An easy treatment of hanging nodes in hp-finite elements," *Finite Elements Anal. Des.*, vol. 121, pp. 101–117, Nov. 2016.

[8] A. Díaz-Morcillo, L. Nuño, J. V. Balbastre, and D. Sánchez-Hernández, "Adaptive mesh refinement in electromagnetic problems," in *Proc. 9th Int. Meshing Roundtable*, New Orleans, LA, USA, Oct. 2000, pp. 147–155.

[9] S. Yuan, Y. Dong, Q. Xing, and N. Fang, "Adaptive finite element method of lines with local mesh refinement in maximum norm based on element energy projection method," *Int. J. Comput. Methods*, vol. 17, no. 4, May 2020, Art. no. 1950008.

[10] M. Salazar-Palma, T. K. Sarkar, L.-E. Garcia-Costillo, T. Roy, and A. Djordjevic, *Iterative and Self-Adaptive Finite-Elements in Electromagnetic Modeling*. Norwood, MA, USA: Artech House, 1998.

[11] J. A. T. Vásquez, F. Vipiana, Z. Peng, J.-F. Lee, and G. Vecchi, "An automatic *h*-refinement scheme for discontinuous Galerkin integral equations in the analysis of multi-scale structures," in *Proc. 7th Eur. Conf. Antennas Propag. (EuCAP)*, Gothenburg, Sweden, Apr. 2013, pp. 4048–4049.

[12] A. Das and D. Gope, "Adaptive mesh refinement for fast convergence of EFIE-based 3-D extraction," *IEEE Trans. Compon., Packag., Manuf. Technol.*, vol. 5, no. 3, pp. 404–414, Mar. 2015.

[13] S. K. Kim and A. F. Peterson, "Adaptive *h*-refinement for the RWG-based EFIE," *IEEE J. Multiscale Multiphys. Comput. Techn.*, vol. 3, pp. 58–65, 2018.

[14] P. I. Cilliers and M. M. Botha, "Goal-oriented error estimation for the method of moments to compute antenna impedance," *IEEE Antennas Wireless Propag. Lett.*, vol. 19, no. 6, pp. 997–1001, Jun. 2020.

[15] P. I. Cilliers and M. M. Botha, "Results in goal-oriented error estimation for MoM input impedance computation," in *Proc. IEEE Int. Symp. Antennas Propag. North Amer. Radio Sci. Meeting*, Montréal, QC, Canada, Jul. 2020, pp. 1055–1056.

[16] J. A. Tobon Vasquez, Z. Peng, J.-F. Lee, G. Vecchi, and F. Vipiana, "Automatic localized nonconformal mesh refinement for surface integral equations," *IEEE Trans. Antennas Propag.*, vol. 68, no. 2, pp. 967–975, Feb. 2020.

[17] S. Cui, J. Bai, S. Yang, and D. Su, "Adaptive error control in method of moments for electromagnetic scattering analysis," in *Proc. Int. Appl. Comput. Electromagn. Soc. (ACES-China) Symp.*, Jul. 2021, pp. 1–2.

[18] S. K. Kim and A. F. Peterson, "Adaptive *h*-refinement for the RWG EFIE applied to targets with edges," *IEEE Trans. Antennas Propag.*, vol. 70, no. 3, pp. 2370–2374, Mar. 2022.

[19] C. Díaz-Cáez, "Fast and efficient electromagnetic simulation of electrically extra-large problems using phase information and mesh automation," Ph.D. dissertation, Dept. Elect. Eng. Comput. Sci., Howard Univ., Washington, DC, USA, 2022.

[20] Z. Peng, K.-H. Lim, and J. Lee, "A discontinuous Galerkin surface integral equation method for electromagnetic wave scattering from nonpenetrable targets," *IEEE Trans. Antennas Propag.*, vol. 61, no. 7, pp. 3617–3628, Jul. 2013.

[21] V. F. Martín, L. Landesa, F. Obelleiro, and J. M. Taboada, "A discontinuous Galerkin combined field integral equation formulation for electromagnetic modeling of piecewise homogeneous objects of arbitrary shape," *IEEE Trans. Antennas Propag.*, vol. 70, no. 1, pp. 487–498, Jan. 2022.

[22] W. C. Chew, J.-M. Jin, E. Michielssen, and J. M. Song, *Fast and Efficient Algorithms in Computational Electromagnetics*. Norwood, MA, USA: Artech House, 2001.

[23] Y. Wang, S. Yan, and Z. Nie, "A point-adaptive grouping scheme of MLFMA for electrically large scattering simulation," *IEEE Trans. Antennas Propag.*, vol. 64, no. 12, pp. 5527–5530, Dec. 2016.

[24] C. Díaz-Cáez and S. Yan, "A pattern-recognition-based mesh refinement method for the moment method analysis of electromagnetic scattering problems," in *Proc. IEEE Int. Symp. Antennas Propag. USNC-URSI Radio Sci. Meeting (AP-S/URSI)*, Denver, CO, USA, Jul. 2022, pp. 1136–1137.

[25] C. Díaz-Cáez and S. Yan, "An automated adaptive h-Refinement technique for solving SIEs with nonconformal meshes," in *Proc. Int. Appl. Comput. Electromagn. Soc. Symp. (ACES)*, Monterey, CA, USA, Mar. 2023, pp. 1–2.

[26] C. Díaz-Cáez and S. Yan, "Traveling and standing wave recognition based on PE basis functions and standing wave ratio," in *Proc. IEEE Int. Symp. Antennas Propag. USNC-URSI Radio Sci. Meeting (USNC-URSI)*, Portland, OR, USA, Jul. 2023, pp. 1–2.

[27] E. Jorgensen, J. L. Volakis, P. Meincke, and O. Breinbjerg, "Higher order hierarchical legendre basis functions for electromagnetic modeling," *IEEE Trans. Antennas Propag.*, vol. 52, no. 11, pp. 2985–2995, Nov. 2004.

[28] J. R. Mautz and R. F. Harrington, "H-field, E-field, and combined-field solutions for conducting bodies of revolution," *Arch. Elektron. Ubertragungstech.*, vol. 32, no. 4, pp. 159–164, 1978.

Christian O. Díaz-Cáez (Member, IEEE) received the B.S.E.E. degree from Universidad Del Turabo, Gurabo, Puerto Rico, in 2016, and the M.Eng. and Ph.D. degrees in electrical engineering from Howard University, Washington, DC, USA, in 2019 and 2022, respectively.

He is currently a Radar Imagery Scientist with the United States Department of Defense, specializing in Synthetic Aperture Radar (SAR). He has participated in research at different universities and government research institutions such as The Massachusetts Institute of Technology Lincoln Laboratory, Lexington, MA, USA, in 2021, Tsinghua University, Beijing, China, in 2019, The Johns Hopkins University Applied Physics Laboratory, Laurel, MD, in 2018, and The Joint Center for Satellite Data Assimilation and National Oceanic and Atmospheric Administration, Boulder, CO, USA, in 2015. His research in computational electromagnetics (CEM) focuses on areas such as the modeling and simulation of electromagnetic scattering, radiation, and the evaluation of radar cross section (RCS). He is also interested in advanced numerical methods in CEM, particularly integral-equation-based methods, fast algorithms, and large-scale parallel computing techniques.

Dr. Díaz-Cáez has received numerous awards and fellowships, including the DoD SMART SEED Grant Early Career Award, the National Science Foundation (NSF) LSAMP Fellowship, the Department of Defense SMART Scholarship, and the Intel Graduate Scholarship. He is also a reviewer for multiple conferences such as the IEEE International Symposium on Antennas and Propagation, and the International Applied Computational Electromagnetics Society (ACES) Symposium.

Su Yan (Senior Member, IEEE) received the B.S. degree in electromagnetics and microwave technology from the University of Electronic Science and Technology of China, Chengdu, China, in 2005, and the M.S. and Ph.D. degrees in electrical and computer engineering from the University of Illinois at Urbana–Champaign (UIUC), Urbana, IL, USA, in 2012 and 2016, respectively.

From August 2016 to July 2018, he was a Post-Doctoral Research Associate and an Instructor with the Department of Electrical and Computer Engineering, UIUC. He joined the Howard University, Washington, DC, USA, as an Assistant Professor in August 2018. He has been the Director of Graduate Studies of the Department of Electrical Engineering and Computer Science, since June 2020, and the Director of the IBM-HBCU Quantum Center since October 2023. He has authored or coauthored over 120 papers in refereed journals and conferences, three book chapters, and one edited book. His current research interests include nonlinear electromagnetic and multiphysics problems, extreme-scale and multiscale algorithms for electromagnetic scattering and radiation, numerical methods in electromagnetic design, optimization, computational imaging, and machine learning for scientific computing.

Dr. Yan is a Full Member of the USNC-URSI Commission B and a Life Member of the Applied Computational Electromagnetics Society (ACES). He was a recipient of the NSF Early Career Award in 2023, the ACES Early Career Award "for contributions to linear and nonlinear electromagnetic and multiphysics modeling and simulation methods" by ACES in 2020, the P. D. Coleman Outstanding Research Award and the Yuen T. Lo Outstanding Research Award by UIUC, in 2014and 2015, respectively. He was also a recipient of the Edward E. Altschuler AP-S Magazine Prize Paper Award by the IEEE Antennas and Propagation Society in 2020, the Best Student Paper Award (The First Place Winner) at the IEEE ICWITS/ACES 2016 Conference, Honolulu, HI, USA, in 2016; the USNC/URSI Travel Fellowship Grant Award by the National Academies in 2015, the Best Student Paper Award (The First Place Winner) at the 27th International Review of Progress in ACES, Williamsburg, VA, USA, in 2011, and the Best Student Paper Award by the IEEE Chengdu Section in 2010. He serves as a Member of the Board of Directors of ACES from 2024 to 2027. He serves as an Associate Editor for *IEEE ACCESS* and the *International Journal of Numerical Modeling: Electronic Networks, Devices and Fields*, and a reviewer for multiple journals and conferences. He also served as the Chair/a member of the Organizing Committee and the Technical Program Committee and a Session Organizer for numerous international conferences.